The effect of addition of hardystonite on the strength, ductility and corrosion resistance of WE43 magnesium alloy

Eivani, A. R.; Tabatabaei, F.; Khavandi, A. R.; Tajabadi, M.; Mehdizade, M.; Jafarian, H. R.; Zhou, J.

DOI
10.1016/j.jmrt.2021.05.027

Publication date
2021

Document Version
Final published version

Published in
Journal of Materials Research and Technology

Available online at www.sciencedirect.com

jmr&t Journal of Materials Research and Technology

journal homepage: www.elsevier.com/locate/jmrt

Original Article

The effect of addition of hardystonite on the strength, ductility and corrosion resistance of WE43 magnesium alloy

A.R. Eivani [a,*], F. Tabatabaei [a], A.R. Khavandi [a], M. Tajabadi [a], M. Mehdizade [a], H.R. Jafarian [a], J. Zhou [b]

[a] School of Metallurgy and Materials Engineering, Iran University of Science and Technology, Tehran, Iran
[b] Department of Biomechanical Engineering, Delft University of Technology, Mekelweg 2, Delft, 2628 CD, the Netherlands

ARTICLE INFO

Article history:
Received 5 January 2021
Accepted 19 May 2021
Available online 1 June 2021

Keywords:
Magnesium
Hardystonite
Nanocomposite
Friction stir processing
Corrosion properties

ABSTRACT

A composite material based on the WE43 magnesium alloy and containing nano-sized hardystonite ceramic particles was processed by means of friction stir processing (FSP). Compressive strength and strain-at-failure of the WE43 alloy increased as a combined result of FSP and nanoparticle reinforcement. The results of potentiondynamic polarization and electrochemical impedance spectroscopy tests indicated that the corrosion mechanism of the nanocomposite is combination of uniform corrosion and localized pitting corrosion which is not different from the base metal. However, the corrosion rate is significantly decreased as a result of reduced localized corrosion of the base metal after FSP and the effect of hardystonite to reduce pitting corrosion. The polarization resistance is increased from 192.48 to 339.61 and 1318.12 Ω/cm^2 by applying FSP on WE43 and addition of nano-sized hardystonite particles, respectively. Indeed, the fabricated nanocomposite shows significantly increased corrosion resistance. Enhanced strength, ductility and corrosion resistance were attributed to grain refinement in addition to the fragmentation and redistribution of second-phase particles in the magnesium matrix, occurring during FSP.

1. Introduction

Magnesium is a metal with a low density, compared to other metals for structural applications, and a moderate strength, thus possessing a high strength-to-weight ratio. As such, it has been extensively used across a broad scope of industrial sectors where light weighting is essential. Its large standard potential, i.e., −1.63 V, however, makes it to corrode fast, once in electric contact with another metal in an electrolyte by forming a galvanic cell and mostly acting as sacrificial anode. The high corrosion rate of magnesium has been considered to

* Corresponding author.
E-mail address: aeivani@iust.ac.ir (A.R. Eivani).
https://doi.org/10.1016/j.jmrt.2021.05.027

be an advantage, if it is used as an implant material that degrades over time in physiological environments. On the other hand, the biodegradation of magnesium implant is accompanied by the reductions in its mechanical properties over time and even the loss in its structural integrity. Therefore, the corrosion performance of biodegradable implant should be adjusted in such a way that its structure stays integrated during the healing of the host bone tissue when its mechanical load-bearing capacity is needed. In addition, it has been reported that rapid degradation of magnesium implant causes rapid release of H_2 gas, especially within a short period of time upon implantation, which is hazardous by itself [1]. If the gas release process is fast, the surrounding tissues may not be able to absorb it. As a result, H_2 gas accumulates, causing local swelling [2–4] and negatively affects the bone healing process [2,5]. Therefore, for magnesium to be used as a clinically acceptable biodegradable implant material, a critically important issue to resolve is to increase its corrosion resistance in physiological environments, thereby flattening the H_2 gas evolution curve and maintaining its mechanical functionality during the bone healing process. In addition to a large standard potential, two other causes are widely known to be responsible for the low corrosion resistance of magnesium, i.e., (i) the oxide film on the magnesium surface being not really protective and (ii) the impurities and secondary phases in magnesium causing galvanic corrosion [6]. Secondary phases in common commercial-grade magnesium alloys are mostly $Mg_{17}Al_{12}$ [7–10], AlMn [6], Al_8Mn_5 [11], $Mg_{12}Nd$ [12] and Mg_2Pb [9]. Depending on the type of secondary phases, sizes, number density and morphology, however, the corrosion resistance of magnesium can possibly be improved to some extent by alloying. For example, Al [9,11], Mn [11], Zr [10] and rare earth elements [13] have been added to magnesium partly for the sake of improving its corrosion resistance.

Another issue that has been encountered in applying magnesium for engineering applications as well as for biomedical applications concerns its low ductility at or near room temperature, leading to premature failure and even catastrophic failure under complex stress conditions. The low ductility is attributed to the small number of operating slip systems of magnesium with a hexagonal close-packed (hcp) crystal structure. In addition, the presence of brittle secondary phases at the grain boundary regions can cause poor ductility of magnesium alloys. Furthermore, relatively low strengths of magnesium and its alloys may also limit their applications where load-bearing capabilities are required [14]. It is known that adding 3.7–4.3 wt.% yttrium, and 2.4–4.4 wt.% rare earth elements, e.g., neodymium, and 0.4 wt.% zirconium to magnesium to form the WE43 magnesium alloy results in a refined grain structure, enhanced strength and improved corrosion behavior [15]. In addition to elevated-temperature applications as a creep-resistant alloy (up to 250 °C), WE43 with a favorable biodegradation rate, compared to pure magnesium and other magnesium alloys, has been considered to be the most popular metallic material for biodegradable medical applications. It has been found that the grain structure, precipitation and distribution of second-phase particles in the alloy as well as texture formation are strongly dependent on the fabrication process [15]. Consequently, the resulting mechanical properties, e.g., yield and ultimate tensile/compressive strengths and ductility are all affected by the method and condition of material processing [15].

Although the WE43 alloy has already made inroads into the biomedical industry in the form of implantable medical devices, e.g., biodegradable cardiovascular stents [16–19] and orthopedic implants [20–22], its main limitations are well recognized and many issues, most notably, macroscopic pitting, high corrosion rate and macropitted nano phasic degradation [14], are yet to be resolved. In addition, the alloy does not offer sufficient mechanical properties, as required in many load-bearing orthopedic applications.

The aim of the present research was to address the abovementioned limitations of the WE43 alloy by adding bioactive hardystonite nanoparticles to the alloy to form a nanocomposite and to understand how the mechanical properties and corrosion resistance of the nanocomposite could be affected by material processing. Composites and nanocomposites with improved mechanical properties, corrosion resistance and tribological performance have been previously produced and the approach seems to be a realistic and efficient method to acquire required properties [23–33]. Fabrication of the composite has, in some cases, been combined by structural modifications using severe plastic deformation techniques and in specific, friction stir processing (FSP) [34,35]. The main goal of this research is modification and improvement of mechanical and corrosive properties of WE43 based bio composites with possible biomedical applications. So, in this study, to refine the grain structure, redistribute second-phase particles and disperse nano-sized ceramic particles, FSP is used. For comparison purposes, the monolithic WE43 alloy was subjected to the same FSP and subsequent tests.

2. Materials and experimental procedures

Hot-rolled WE43 magnesium plates with a thickness of 10 mm and the chemical composition shown in Table 1, detected by EDS, were used as the starting material in this research. The plates were annealed at 440 °C for 3 h and cut into rectangular samples with sizes of 140 × 50 mm^2. For each sample, a groove with a width of 1 mm and a depth of 2 mm was created in the length direction by machining to allow the placement of reinforcing agent. Schematic illustrations of the FSP set-up and process procedures are given in Fig. 1. Prior to FSP, samples were cleaned and degreased in acetone for 30 min and dried by using blowing air.

A Zn- and Ca-containing silicate-based bioceramic powder, i.e., hardystonite ($Ca_2ZnSi_2O_7$), was used as the reinforcing

Table 1 – Chemical composition of the WE43 magnesium alloy used as the starting material in this investigation.

Element	Mg	Zn	Y	Zr	Sc	Ce	Nd	Gd
Wt. %	Balance	0.08	3.72	0.41	1.47	0.13	2.13	1.11

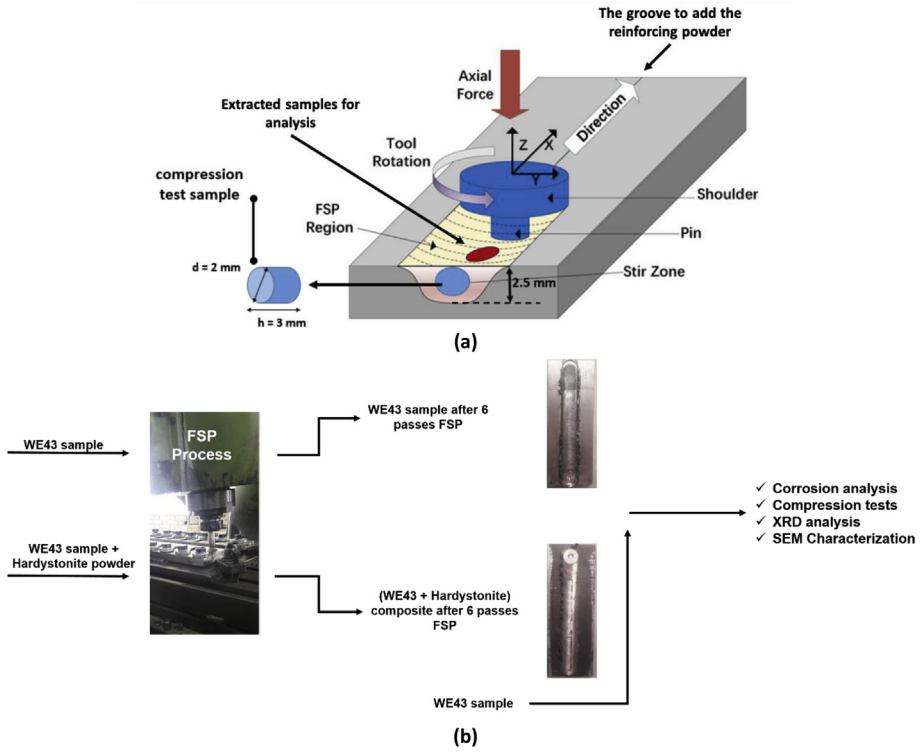

Fig. 1 – Schematic illustrations of (a) the FSP and the regions at which the test samples were extracted and (b) process procedures.

agent and imbedded into the WE43 alloy through FSP. The powder was characterized by using a DRON-8 X-ray diffractometer (XRD) operating at 40 KV and 30 mA. The sizes and morphology of ceramic nanoparticles were determined by using a TESCAN VEGA/XMU scanning electron microscope (SEM). In order to minimize agglomeration of nanoparticles, prior to placing the powder in the grooves of the WE43 plate samples, powder particles were dried, followed by dispersion in ethanol using an ultrasonic stirrer.

After the hardystonite powder was placed in the groove, the groove was flattened by using a pin-less cylindrical tool with a diameter of 15 mm in order to confine the added powder during FSP. A tool with a shoulder diameter of 15 mm, a pin height of 2.5 mm and a pin diameter of 3.5 mm was used for FSP. FSP was conducted at a pin moving speed of 107 mm/min and a rotational speed of 1180 rpm. The FSP condition was chosen, based on the information available in the open literature concerning the formation of a composite on the one hand and the avoidance of overheating the matrix alloy plate on the other in order to prevent abnormal grain growth and significant deterioration of mechanical properties from occurring [36,37]. The process was repeated for 6 passes to achieve a homogeneous distribution of reinforcing nanoparticles and significant refinement of grains and second-phase particles in the matrix alloy. WE43 alloy samples were subjected to the same FSP. The microstructures were characterized using SEM equipped with an energy dispersive spectrometer (EDS) and the XRD apparatus mentioned earlier. Field emission gun Philips XL30 was also used for characterization of microstructure. Average grain size was determined using line intercept method according to ASTM E112 standard [38].

Uniaxial compression tests at room temperature were conducted to determine the mechanical properties of the FSP materials, according to the ASTM E9 standard [38]. Cylindrical specimens with a diameter of 2 mm and a height of 3 mm were machined along the length of the FSP samples, as shown in Fig. 1. Prior to the tests, both end sides of the specimens were mechanically polished to ensure parallel surfaces with minimum roughness. The tests were carried out using a 50 kN SANTAM universal tensile/compression machine at a cross-head speed of 0.5 mm/min. Stress–strain curves were extracted from load–displacement data. Due to extreme size limit of the specimens, attachment of an extensometer for precise measurement of elastic strain was not possible. Therefore, the elastic section of the stress–strain curves was deleted and the plastic parts were presented.

The corrosion behaviors of the materials were investigated by performing electrochemical impedance spectroscopy (EIS) and potentiodynamic polarization tests, according to the ASTM B457-67 and ASTM G102-98-E1 standards, respectively. The electrochemical tests were conducted in simulated body fluid (SBF) using a Princeton Applied Research potentiostat apparatus (model Versa Stat 4) on a sample with 10 mm^2 surface area. The electrochemical evaluation was performed using a three-electrode cell at room temperature. The sample was set as the working electrode, and the counter and reference electrodes were platinum rod and saturated calomel (SC),

respectively. The samples were kept in the SBF solution for 20 min prior to the start of the tests in order to achieve a stable potential. The stable condition was set when no more than ±5 μV variations occurred during 5 min measurement of potential. Scan rate was 1 mV/S and scan started −0.25 V below open circuit potential (OCP) and ended at reference electrode potential (SCE). Corrosion current density and corrosion potential were calculated, based on the Tafel extrapolation of the anodic and cathodic branches. Electrochemical impedance tests were performed over a range of frequencies from 10 mHz to 100 kHz with an amplitude voltage of 10 mV and the experimental results were fitted by using the ZSimWin 3.21 software.

3. Results and discussion

The utilized tests to scrutinize variation of the manifold properties of samples by performing FSP process and adding hardystonite nano-particles are discussed in this section.

3.1. Characteristics of the starting materials

The microstructure of the WE43 magnesium alloy after annealing at 440 °C for 3 h is shown in Fig. 2. It can be seen that the alloy was fully recrystallized and its microstructure was composed of nearly equiaxed fine grains with a size range of 10–40 μm and second-phase particles. The average grain size of the sample was 18 μm according to ASTM E112 [38]. A large number density of second-phase particles with blocky and rod-like morphologies were present inside the grains. When the microstructure of the as-annealed alloy was observed at a higher magnification, as shown in Fig. 2(b), it became clear that second-phase particles were also located nearby and along the grain boundaries.

An SEM micrograph and the XRD pattern of the hardystonite powder used in this investigation are shown in Fig. 3. It can be seen that the sizes of nanoparticles were in general smaller than 100 nm, although a few coarse particles in the size range of 200–300 nm were observable. The XRD pattern of the powder shown in Fig. 3(b) confirmed that indeed it was purely composed of hardystonite, according to JCPDS: 01-075-0916 card.

3.2. Distribution of nanoparticles in the nanocomposite

An SEM micrograph of the FSP nanocomposite showing the distribution of nanoparticles in SZ [34], corresponding elemental distribution maps and a typical EDS spectrum of particle clusters are presented in Fig. 4. The EDS maps confirmed the presence of the elements that composed hardystonite, i.e., Zn, Ca, Si and O in the FSP composite. The EDS maps also showed two coarse particles at the upper left part of FSP nanocomposite sample, containing Ca, Zn, O and Si of higher concentrations than those in the matrix alloy, thus being hardystonite particles. Considering the fact that all nanoparticles were less than 300 nm in size, as shown in Fig. 3(a), one could infer that agglomeration of nanoparticles and formation of nanoparticle clusters occurred during FSP, which could negatively affect the reinforcing effect of nanoparticles on mechanical properties [34]. It was also observed that the distribution of nanoparticles was not really homogeneous. The inhomogeneity in nanoparticle distribution could also affect the mechanical properties negatively. The extent of the negative effects of nanoparticle dispersion on mechanical properties needs to be further studied.

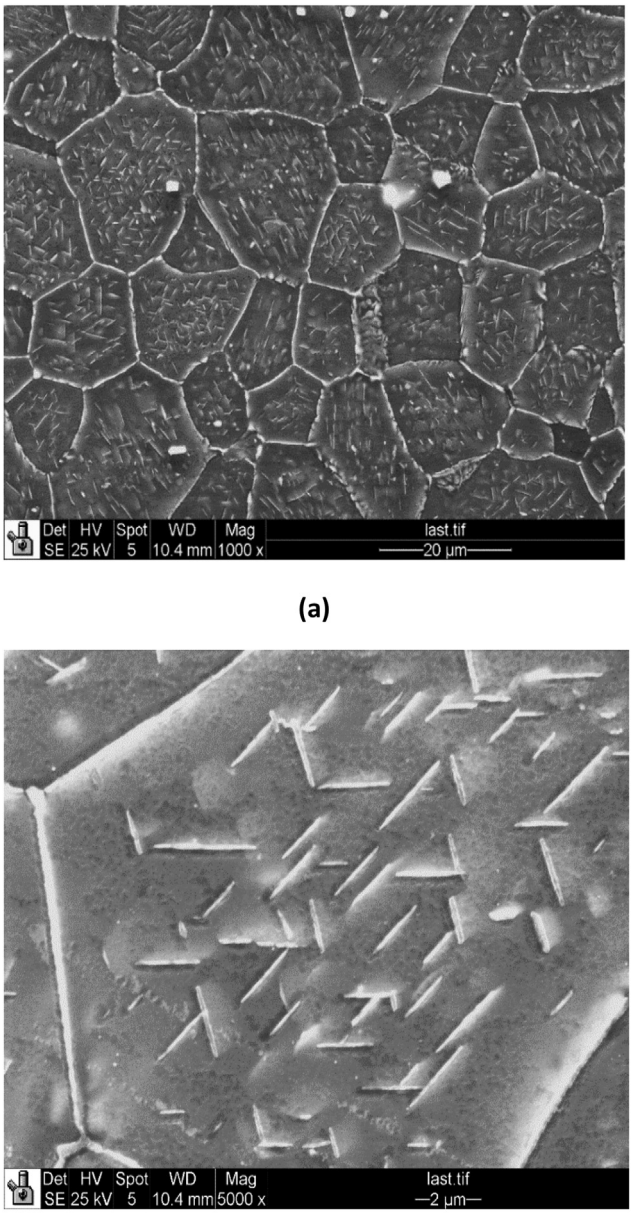

Fig. 2 – (a) low- and (b) high-magnification micrographs showing the as-annealed grain structure of the WE43 magnesium alloy and second-phase particles.

3.3. Mechanical properties of the FSP nanocomposite

Stress–strain curves of the as-annealed WE43, FSP WE43 alloy and FSP nanocomposite obtained from uniaxial compression tests at room temperature are shown in Fig. 5. It can be clearly

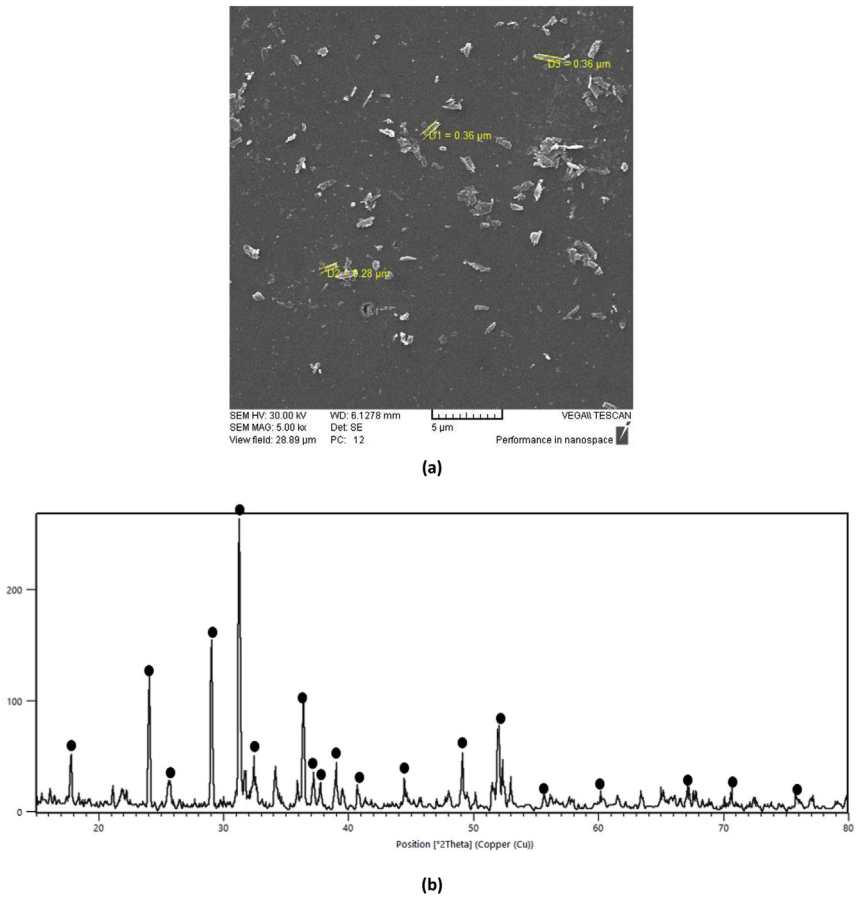

Fig. 3 – (a) SEM micrograph and (b) XRD pattern of the hardystonite powder. The black circles on the XRD pattern correlate to hardystonite.

seen that the FSP nanocomposite possessed both improved compressive strength and ductility, in comparison with those of the as-annealed WE43 alloy. Improvements in strength and ductility were also achieved in the case of the FSP WE43 alloy, which could be attributed to grain refinement, second-phase particle fragmentation and redistribution occurring during FSP. As observable in Fig. 2, second-phase particles dispersed continuously along the grain boundaries in the as-annealed WE43 alloy. Such a distribution of second-phase particles could negatively affect the mechanical properties of the alloy. Their fragmentation and redistribution occurring during FSP could be greatly beneficial to the mechanical properties. This finding agrees with the observation that mechanical properties and even corrosion resistance of many magnesium alloys could be improved by applying severe plastic deformation by making use of grain refinement and fragmentation and redistribution of second-phase particles located at grain boundaries [39–43].

3.4. *Corrosion behavior of the FSP nanocomposite*

The corrosion behavior of different samples are analyzed via potentiondynamic polarization and electrochemical impedance spectroscopy tests which are discussed in detail hereunder.

3.4.1. *Polarization behavior*

The potentiondynamic polarization curves of different samples after polishing and drying are shown in Fig. 6. The values of i_{corr} (corrosion current density), E_{corr} (corrosion potential), β_a (the rate of anodic reactions) and β_c (the rate of cathodic reactions) were calculated by drawing tangent lines on the linear part of the anodic and cathodic branches. These values together with *mpy* (corrosion rate) and R_p (polarization resistance) are listed in Table 2. The *mpy* value, representing the weight loss per year as an indicator of corrosion rate in the SBF solution, was calculated by using Eq. (3) [44]:

$$mpy = \frac{0.00327 \times i_{corr} \times (E.W)}{n \times \rho} \quad (3)$$

In this equation, n is the number of electrons exchanged in the dissolution reaction, which is +2 for Mg, ρ the density of magnesium (1.738 g/cm^3), and $E.W$ the equivalent weight of magnesium (24.312 g). R_p represents the polarization resistance of the sample and can be calculated using Eq. (4) [45]:

$$R_p = \frac{1}{2.303\left(\frac{1}{\beta_a} + \frac{1}{\beta_c}\right) i_{corr}} \quad (4)$$

For Mg alloys, the cathodic reaction in the SBF solution is the hydrogen evolution that consumes the electrons of H^+ (or

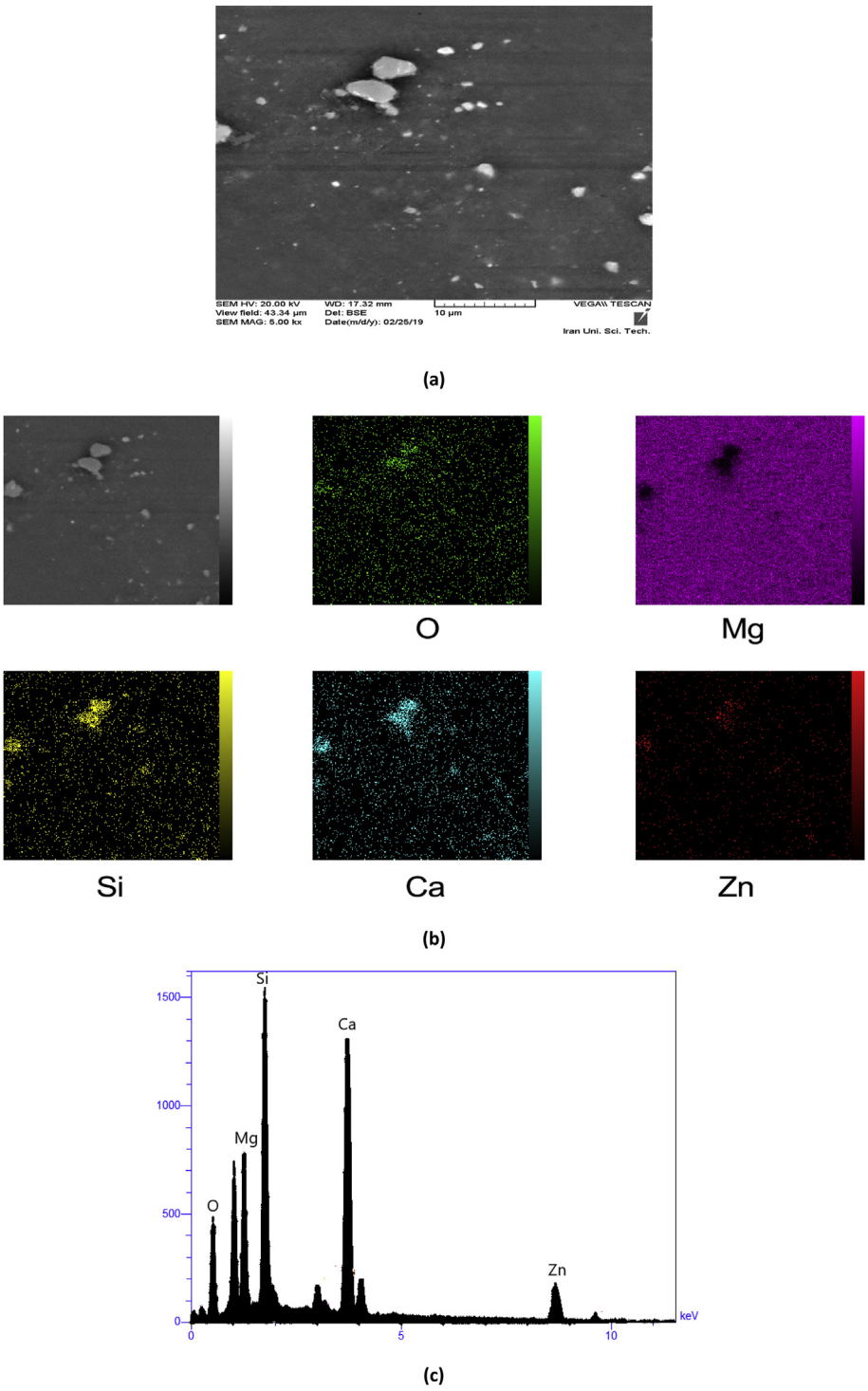

Fig. 4 – (a) SEM micrograph showing the distribution of nanoparticles in FSP nanocomposite sample, (b) corresponding elemental distribution maps and (c) a typical EDS spectrum of hardystonite particle clusters surrounded by magnesium.

H_3O) cations (dissociation of water) on magnesium surface according to Eq. (5) [46,47]:

$$2H^+ + 2e^- = H_2 \text{ (cathodic reaction)} \quad (5)$$

In addition, the anodic reaction is the dissolution of magnesium at the interface of Mg surface-SBF electrolyte according to Eq. (6) [46,47]:

$$2\,Mg = 2Mg^{2+} + 4e^- \text{ (anodic reaction)} \quad (6)$$

and finally, MgO or $Mg(OH)_2$ may be generated on the surface of the substrate as a protective layer, according to Eqs. (7) and (8) [46,47]:

$$Mg + O = MgO \quad (7)$$

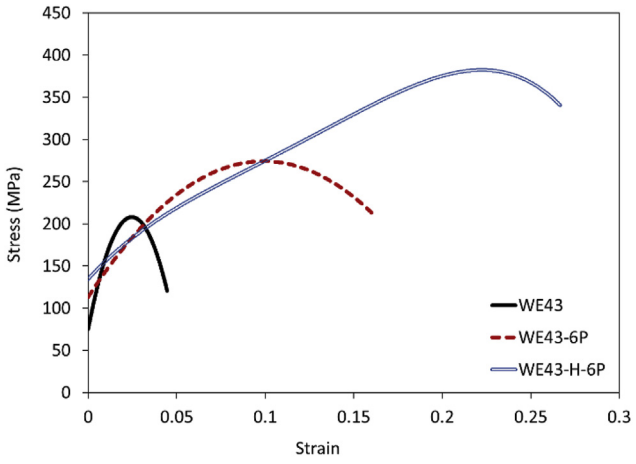

Fig. 5 – Stress–strain curves acquired from compression tests.

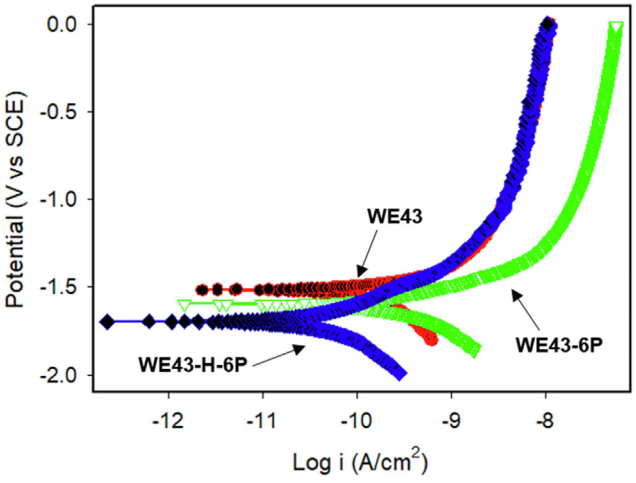

Fig. 6 – Potentiodynamic polarization curves of WE43, WE43-6P and WE43-H-6P samples.

$$Mg^{2+} + 2OH^{-} = Mg(OH)_2 \quad (8)$$

It can be seen in Table 2 that as a result of applying FSP to the WE43 alloy, the values of I_{corr} and *mpy* decreased and R_p increased, compared to those of the as-annealed counterpart. Thus, FSP indeed led to improvements in corrosion resistance due to the fragmentation and redistribution of second-phase particles in the WE43 alloy. By adding hardystonite nanoparticles to the FSP WE43 alloy, I_{corr} and *mpy* reduced further from 141.496 to 33.391 μA/cm^2 and from 3.166 to 0.747 mm per year, respectively, and R_p increased from 339.61 up to 1318.12 Ω/cm^2. It is therefore clear that by adding hardystonite nanoparticles the corrosion resistance of the FSP WE43 alloy could be improved further. It is likely that the susceptibility of the as-annealed WE43 alloy to pitting corrosion could be reduced by applying FSP. This is because that during FSP second-phase particles were greatly refined to such an extent that the effect of such particles to act as the origins of pitting corrosion would be diminished. As a result of an increase in particle number density and decreases in particle size, the uniformity of the distribution of second-phase particles was improved. Consequently, corrosion pits generated on surface would become less stable, mostly re-passivate and disappear. This would result in more uniform corrosion occurring on the surface of the FSP WE43 alloy in comparison to the as-annealed counterpart. As shown in Fig. 7 the corroded surface of FSP WE43 alloy sample is more uniform than that of the as-annealed sample. In addition, the corroded surface of the FSP nanocomposite sample is more uniform than that of the FSP monolithic WE43 alloy sample. With the dispersion of hardystonite nanoparticles in the FSP WE43 alloy, pitting corrosion resistance could be further improved, with the polarization resistance value reaching 1318.12 Ω/cm^2, which is in line with the high corrosion resistance of hardystonite nanoparticles, as these particles could act as obstacles to the corrosion reaction, provided that strong bonding with the matrix was achieved. Moreover, adding hardystonite nanoparticles to the WE43 alloy led to lessened generation of deep pits.

3.4.2. *EIS characteristics*

The Nyquist, bode, and bode phase plots of the as-annealed WE43 alloy, FSP WE43 alloy and FSP nanocomposite are shown in Fig. 8. It can be seen in Fig. 8(a) that the Nyquist diagram includes two capacitive loops and an inductive loop. One of the two capacitive loops correlates to the passive layer that is generated near the surface of the sample and indicates its corrosion resistance. The other one is correlated to the transition of electrical charge at the magnesium-SBF electrolyte interface (double electrical layer). As previously mentioned, the experimental EIS data were fitted by using the ZSimWin 3.21 software. The simulated equivalent circuit diagram, R_{sol} (C_PR_P) (Q_{dl} (R_t ($L_{Pit}R_{Pit}$))), is shown in Fig. 9.

In the obtained equivalent circuit, R_{sol} is the electrical resistive behavior of the SBF solution, C_p and R_p are the electrical capacitive behavior and electrical resistive of the passive layer, respectively. L_{pit} and R_{pit} represent the inductive behavior of pits that may be related to second-phase particles in the WE43 alloy, C_{dl} represents the electrical capacitive behavior of the double electrical layer and R_t is the charge transfer resistive behavior of the substrate-passive layer interface. The values of these electrochemical parameters

Table 2 – Values of electrochemical parameters obtained from potentiodynamic polarization analysis.

sample	I_{Corr} (μA/cm^2)	E_{Corr} (V)	βa (mV.dec^{-1})	$-\beta c$ (mV.dec^{-1})	Rp (Ω/cm^2)	*mpy* (mm/year)
WE43	206.161	−1.602	160.413	211.37	192.48	4.613
WE43-6P	141.496	−1.536	172.375	306.787	339.61	3.166
WE43-H-6P	33.391	−1.691	193.748	209.984	1318.12	0.747

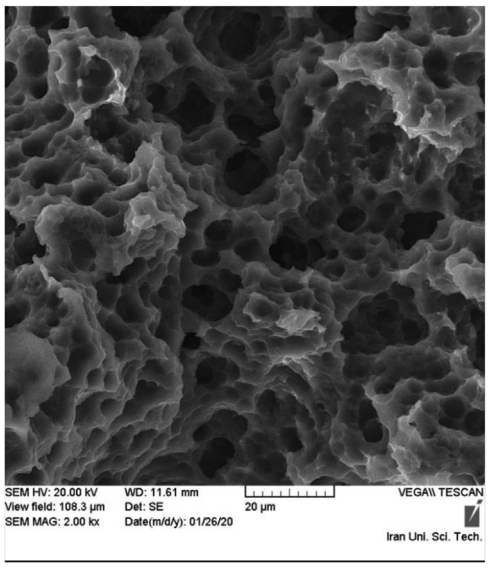

(a)

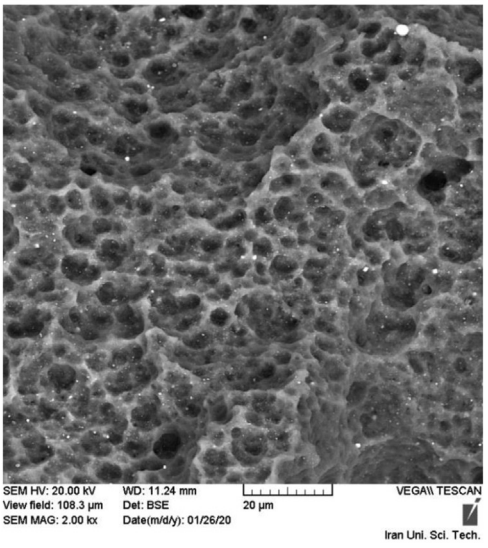

(b)

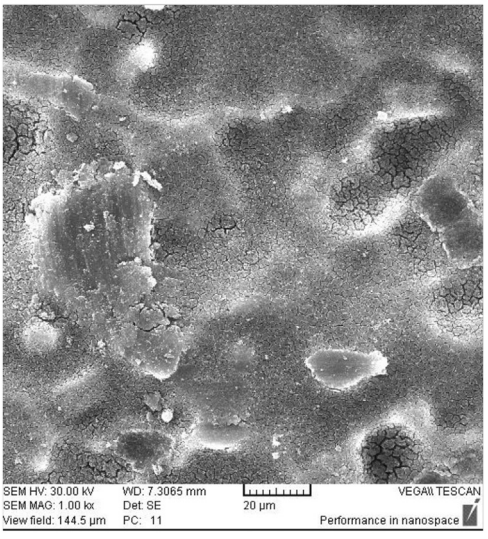

(c)

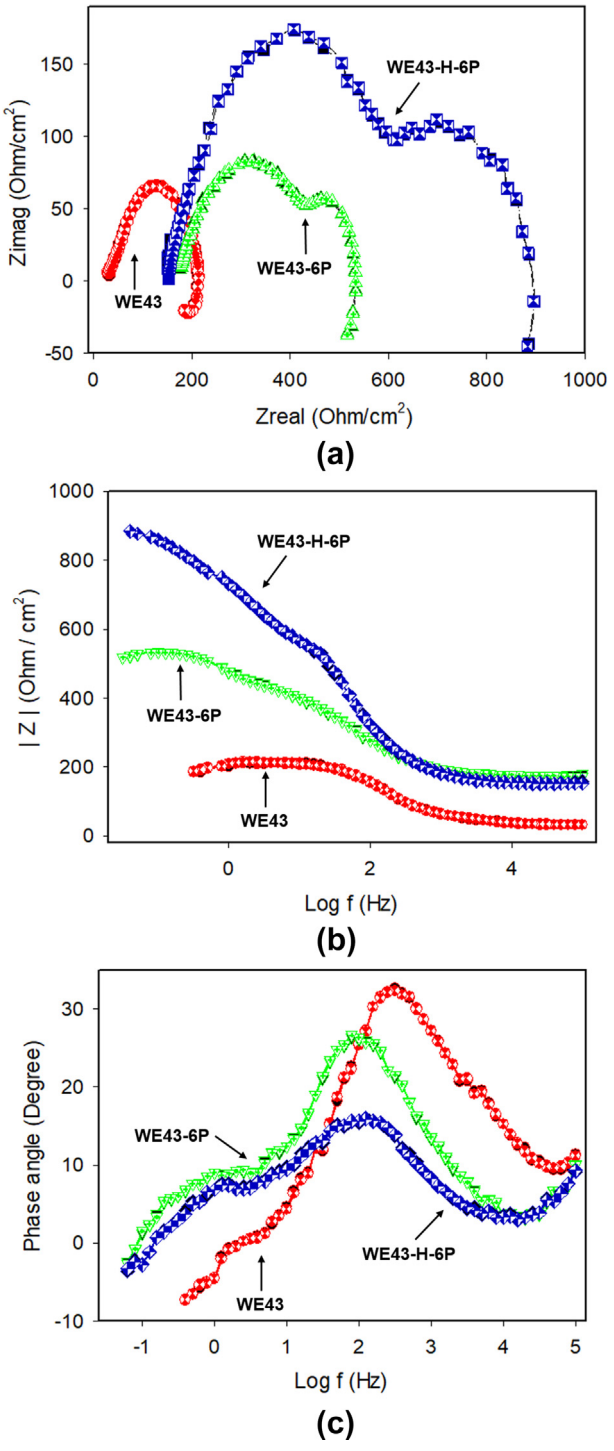

Fig. 8 – (a) Nyquist, (b) bode and (c) bode phase plots of WE43, WE43-6P and WE43-H-6P samples.

were calculated from the experimental EIS data and are reported in Table 3. There is a good agreement between the measured data points and the fitted data, which indicates the

Fig. 7 – Surface of (a) WE43, (b) WE43-6P and (c) WE43-H-6P samples corroded during immersion in the SBF solution.

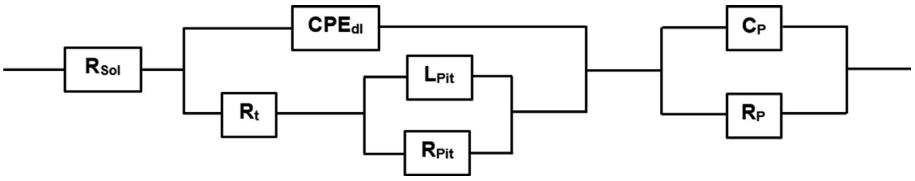

Fig. 9 – Obtained equivalent circuit diagram of the fitted EIS data by using the ZsimpWin 3.21 software.

suitability of the chosen equivalent circuit and the software for fitting. The values of fitting error (K_{square}) for WE43, FSP WE43 and FSP nanocomposite samples are 5.18×10^{-5}, 2.58×10^{-5} and 3.15×10^{-5}, respectively. The equivalent circuit includes a constant phase element (CPE) parameter for the double electrical layer, in which CPE_{dl} indicates the dielectric properties of the double electrical layer that represents the amount of deviation from the ideal capacitive behavior and the inhomogeneity of sample surface [48,49]. In addition, the Nyquist diagram includes one inductive loop, which is related to the inductive behavior of pits at low frequencies. The capacitor impedance can be calculated using Eq. (9)

$$Z = 1/j\omega C \tag{9}$$

Moreover, the value of the CPE parameter can be obtained from the experimental EIS data in low frequencies (about 0.01–10 Hz) using Eq. (10)

$$Z_{CPE} = (Q(j\omega)^{\alpha})^{-1} \tag{10}$$

where C is the capacity of the capacitor, ω the angular frequency, j the imaginary $\sqrt{-1}$ and α a constant parameter. It is known that larger capacitive loops indicate higher corrosion resistance. Indeed, Fig. 8(a) shows that the capacitive loop diameter enlarged and corrosion resistance increased as a result of FSP and the addition of hardystonite nanoparticles. As explained earlier, second-phase particle fragmentation occurring during FSP was partly responsible for the increased corrosion resistance of the FSP WE43 alloy. There is no specific and clear definition of the inductive loop, but it is correlated to the absorption and desorption of ions, corrosion products on the surface of the electrode in the solution and specifically generated pits due to the presence of second-phase particles on sample surface.

In addition, because of the fragmentation of second-phase particles during FSP, corrosion reactions on surface became uniform and caused the creation of a more uniform oxide/hydroxide passive layer on surface. Also, the values of R_{pit}, L_{pit} and R_t increased, which could be contributed by a uniform passive layer surrounding fragmented second-phase particles, resulting in an increase in induction resistance and a decrease in pitting corrosion. In other words, decreased sizes of generated pits led to enhanced passive layer uniformity, a reduced CPE value, larger deviation from ideal capacitive behavior, increased equilibrium between corrosion reactions and significantly decreased intensity of galvanic micro couple, and finally improved induction resistance parameter.

The slope of the linear portion of the bode curves in the high frequency range, n, can be used as an acceptable parameter for evaluating the corrosion properties of the samples with a focus on the uniformity of the formed protective passive layer on the surface. From Fig. 8(b), it can be seen that the n value of the WE43 alloy increased by applying FSP and also by adding hardystonite nanoparticles, which was most likely related to high uniformity on the surface of FSP WE43 sample and SFP nanocomposite sample. In FSP WE43 sample (WE43-6P), the sizes of second-phase particles were smaller than those in the as-annealed WE43 sample. In addition to a more uniform passive layer on FSP WE43 sample, fine particles contributed to the protection of the sample and prevention of corrosion reactions. Hardystonite nanoparticles in the FSP WE43-hardystonite nanocomposite (WE43-H-6P) acted as obstacles to further corrosion reactions and related ion exchanges. Therefore, the positive effect of hardystonite nanoparticles led to the further increases in the diameters of capacitive and inductive loops and consequently, a further improvement in corrosion resistance. This was confirmed by the higher n value of WE43-H-6P sample ($n_{WE43} < n_{WE43\ -6P} < n_{WE43\text{-}H\text{-}6P}$), indicating that the surface of a generated passive layer was smoother and more uniform with an effective protective effect.

Moreover, the most important parameter for evaluating corrosion properties in bode phase diagrams is related to the height of single capacitive peak, expressed by the m parameter in this paper. The m value indicates the roughness of surface and its influence on corrosion behavior. As shown, in Fig. 8(c), the m value for WE43, FSP-processed WE43 and nanocomposite samples are 16.08°, 26.34° and 32.64°, respectively. It can be said that the roughness of sample surface was increased by applying FSP and adding hardestonite powder. Therefore, the roughness of FSP nanocomposite sample became higher than other samples and uniformly distributed

Table 3 – Calculated electrochemical parameters of the experimental EIS data.

Sample	R_{sol} (Ohm/cm^2)	$(Q\text{-}m)_{dl}$	R_{dl} (Ohm/cm^2)	R_{pit} (Ohm/cm^2)	$Lpit$ (H/cm^2)	K_{square}
WE43	24.85	0.891	283.25	21.17	141.15	5.18×10^{-5}
WE43-6P	24.72	0.745	364.11	36.85	233.42	2.58×10^{-5}
WE43-H-6P	24.91	0.674	424.37	44.63	381.28	3.15×10^{-5}

particles with a high number density could help lessen destructive corrosive reactions on surface. By considerating n and m values, one can clearly see that the nanocomposite had the highest corrosion resistance in comparison to the monolithic counterpart.

4. Conclusions

In this research, a Mg-based nanocomposite was processed by means of FSP for potential orthopedic implant applications. Bioactive hardystonite ceramic nanoparticles were used to reinforce the WE43 magnesium alloy. The resultant compressive mechanical properties and corrosion resistance of the FSP nanocomposite were evaluated and compared with those of the as-annealed WE43 alloy and FSP WE43 alloy. The results obtained led to the following conclusions.

1 The compressive yield and ultimate strengths of the FSP nanocomposite was about 100% higher than those of the as-annealed monolithic WE43 alloy. The FSP nanocomposite with YS and UTS values of 139 and 380 MPa, respectively, and 27% strain at failure could meet the requirements of implants for load-bearing bone replacement. Therefore, the nanocomposite could be considered to be a suitable candidate material for biodegradable orthopedic implants.
2 Applying FSP process and addition of hardystonite particles led to significantly improved corrosion resistance and increase the polarization corrosion resistance of the WE43 alloy from 192.48 to 339.61 and 1318.12 Ω/cm^2. The FSP nanocomposite had even higher corrosion resistance compared to the FSP WE43 alloy. These improvements in corrosion resistance may be attributed to refined grain structure in addition to fragmented and more uniformly redistributed second-phase particles, which reduced the occurrence of corrosion by the pitting and galvanic mechanisms.

Declaration of Competing Interest

I declare the authors have no competing interests as defined by Nature Research, or other interests that might be perceived to influence the interpretation of the article.

REFERENCES

[1] Li Y, Wen C, Mushahary D, Sravanthi R, Harishankar N, Pande G, et al. Mg–Zr–Sr alloys as biodegradable implant materials. Acta Biomater 2012;8:3177–88. https://doi.org/10.1016/j.actbio.2012.04.028.
[2] Kraus T, Fischerauer SF, Hänzi AC, Uggowitzer PJ, Löffler JF, Weinberg AM. Magnesium alloys for temporary implants in osteosynthesis: in vivo studies of their degradation and interaction with bone. Acta Biomater 2012;8:1230–8.
[3] Witte F, Fischer J, Nellesen J, Vogt C, Vogt J, Donath T, et al. In vivo corrosion and corrosion protection of magnesium alloy LAE442. Acta Biomater 2010;6:1792–9.
[4] Witte F, Kaese V, Haferkamp H, Switzer E, Meyer-Lindenberg A, Wirth CJ, et al. In vivo corrosion of four magnesium alloys and the associated bone response. Biomaterials 2005;26:3557–63.
[5] Kuhlmann J, Bartsch I, Willbold E, Schuchardt S, Holz O, Hort N, et al. Fast escape of hydrogen from gas cavities around corroding magnesium implants. Acta Biomater 2013;9:8714–21.
[6] Zeng R, Zhang J, Huang W, Dietzel W, Kainer KU, Blawert C, et al. Review of studies on corrosion of magnesium alloys. Trans Nonferrous Metals Soc China 2006;16:s763–71.
[7] Makar GL, Kruger J. Corrosion of magnesium. Int Mater Rev 1993;38:138–53.
[8] Song GL, Atrens A. Corrosion mechanisms of magnesium alloys. Adv Eng Mater 1999;1:11–33.
[9] Song G, Atrens A. Understanding magnesium corrosion—a framework for improved alloy performance. Adv Eng Mater 2003;5:837–58.
[10] Song G. Recent progress in corrosion and protection of magnesium alloys. Adv Eng Mater 2005;7:563–86.
[11] Eliezer D, Uzan P, Aghion E. Effect of second phases on the corrosion behavior of magnesium alloys. Mater. Sci. Forum 2003:857–66. Trans Tech Publ.
[12] Guo LF, Yue TM, Man HC. Excimer laser surface treatment of magnesium alloy WE43 for corrosion resistance improvement. J Mater Sci 2005;40:3531–3.
[13] Song G, StJohn D. The effect of zirconium grain refinement on the corrosion behaviour of magnesium-rare earth alloy MEZ. J Light Met 2002;2:1–16.
[14] Shahin M, Munir K, Wen C, Li Y. Magnesium matrix nanocomposites for orthopedic applications: a review from mechanical, corrosion, and biological perspectives. Acta Biomater 2019;96:1–19.
[15] Kubásek J, Dvorskỳ D, Čavojskỳ M, Roudnicka M, Vojtech D. WE43 magnesium alloy–material for challenging applications. Kov. Mater. Mater. 2019;57:159–65.
[16] Bowen PK, Shearier ER, Zhao S, Guillory RJ, Zhao F, Goldman J, et al. Biodegradable metals for cardiovascular stents: from clinical concerns to recent Zn-Alloys. Adv. Healthc. Mater. 2016;5:1121–40.
[17] Hermawan H, Dubé D, Mantovani D. Developments in metallic biodegradable stents. Acta Biomater 2010;6:1693–7. https://doi.org/10.1016/j.actbio.2009.10.006.
[18] Ye CH, Zheng YF, Wang SQ, Xi TF, Li YD. In vitro corrosion and biocompatibility study of phytic acid modified WE43 magnesium alloy. Appl Surf Sci 2012;258:3420–7.
[19] Gu XN, Zhou WR, Zheng YF, Cheng Y, Wei SC, Zhong SP, et al. Corrosion fatigue behaviors of two biomedical Mg alloys–AZ91D and WE43–in simulated body fluid. Acta Biomater 2010;6:4605–13.
[20] Waizy H, Seitz JM, Reifenrath J, Weizbauer A, Bach FW, Meyer-Lindenberg A, et al. Biodegradable magnesium implants for orthopedic applications. J Mater Sci 2013;48:39–50. https://doi.org/10.1007/s10853-012-6572-2.
[21] Waizy H, Diekmann J, Weizbauer A, Reifenrath J, Bartsch I, Neubert V, et al. In vivo study of a biodegradable orthopedic screw (MgYREZr-alloy) in a rabbit model for up to 12 months. J Biomater Appl 2014;28:667–75.
[22] Staiger MP, Pietak AM, Huadmai J, Dias G. Magnesium and its alloys as orthopedic biomaterials: a review. Biomaterials 2006;27:1728–34. https://doi.org/10.1016/j.biomaterials.2005.10.003.
[23] Sadoun AM, Najjar IMR, Abd-Elwahed MS, Meselhy A. Experimental study on properties of Al–Al2O3 nanocomposite hybridized by graphene nanosheets. J. Mater. Res. Technol. 2020;9:14708–17. https://doi.org/10.1016/j.jmrt.2020.10.011.

[24] Abd-Elwahed MS, Ibrahim AF, Reda MM. Effects of ZrO2 nanoparticle content on microstructure and wear behavior of titanium matrix composite. J. Mater. Res. Technol. 2020;9:8528–34. https://doi.org/10.1016/j.jmrt.2020.05.021.
[25] Sadoun AM, Mohammed MM, Fathy A, El-Kady OA. Effect of Al2O3 addition on hardness and wear behavior of Cu–Al2O3 electro-less coated Ag nanocomposite. J. Mater. Res. Technol. 2020;9:5024–33. https://doi.org/10.1016/j.jmrt.2020.03.020.
[26] Sadoun AM, Mohammed MM, Elsayed EM, Meselhy AF, El-Kady OA. Effect of nano Al2O3 coated Ag addition on the corrosion resistance and electrochemical behavior of Cu-Al2O3 nanocomposites. J. Mater. Res. Technol. 2020;9:4485–93. https://doi.org/10.1016/j.jmrt.2020.02.076.
[27] Abd-Elwahed MS, Meselhy AF. Experimental investigation on the mechanical, structural and thermal properties of Cu–ZrO2 nanocomposites hybridized by graphene nanoplatelets. Ceram Int 2020;46:9198–206. https://doi.org/10.1016/j.ceramint.2019.12.172.
[28] Megahed M, Fathy A, Morsy D, Shehata F. Mechanical Performance of glass/epoxy composites enhanced by micro- and nanosized aluminum particles. J Ind Textil 2019:1528083719874479. https://doi.org/10.1177/1528083719874479.
[29] Sadoun AM, Fathy A, Abu-Oqail A, Elmetwaly HT, Wagih A. Structural, mechanical and tribological properties of Cu–ZrO2/GNPs hybrid nanocomposites. Ceram Int 2020;46:7586–94. https://doi.org/10.1016/j.ceramint.2019.11.258.
[30] Fathy A, Abu-Oqail A, Wagih A. Improved mechanical and wear properties of hybrid Al-Al2O3/GNPs electro-less coated Ni nanocomposite. Ceram Int 2018;44:22135–45. https://doi.org/10.1016/j.ceramint.2018.08.326.
[31] Abu-Oqail A, Samir A, Essa ARS, Wagih A, Fathy A. Effect of GNPs coated Ag on microstructure and mechanical properties of Cu-Fe dual-matrix nanocomposite. J Alloys Compd 2019;781:64–74. https://doi.org/10.1016/j.jallcom.2018.12.042.
[32] Wagih A, Abu-Oqail A, Fathy A. Effect of GNPs content on thermal and mechanical properties of a novel hybrid Cu-Al2O3/GNPs coated Ag nanocomposite. Ceram Int 2019;45:1115–24. https://doi.org/10.1016/j.ceramint.2018.10.001.
[33] Sadoun AM, Fathy A. Experimental study on tribological properties of Cu–Al2O3 nanocomposite hybridized by graphene nanoplatelets. Ceram Int 2019;45:24784–92. https://doi.org/10.1016/j.ceramint.2019.08.220.
[34] Bourkhani RD, Eivani AR, Nateghi HR. Through-thickness inhomogeneity in microstructure and tensile properties and tribological performance of friction stir processed AA1050-Al2O3 nanocomposite. Compos B Eng 2019:107061.
[35] Khdair AI, Fathy A. Enhanced strength and ductility of Al-SiC nanocomposites synthesized by accumulative roll bonding. J. Mater. Res. Technol. 2020;9:478–89.
[36] Charit I, Mishra RS. Abnormal grain growth in friction stir processed alloys. Scripta Mater 2008;58:367–71.
[37] Attallah MM, Salem HG. Friction stir welding parameters: a tool for controlling abnormal grain growth during subsequent heat treatment. Mater Sci Eng 2005;391:51–9.
[38] ASTM E112. Standard test methods for determining average grain size E112-10. Astm E112-10 2010;96:1–27. https://doi.org/10.1520/E0112-10.Copyright.
[39] Ben Hamu G, Eliezer D, Wagner L. The relation between severe plastic deformation microstructure and corrosion behavior of AZ31 magnesium alloy. J Alloys Compd 2009;468:222–9.
[40] Silva CL, Oliveira AC, Costa CG, Figueiredo RB, de Fátima Leite M, Pereira MM, et al. Effect of severe plastic deformation on the biocompatibility and corrosion rate of pure magnesium. J Mater Sci 2017;52:5992–6003.
[41] Jiang J, Aibin MA, Saito N, Zhixin S, Dan S, Fumin LU, et al. Improving corrosion resistance of RE-containing magnesium alloy ZE41A through ECAP. J Rare Earths 2009;27:848–52.
[42] Kutniy KV, Papirov II, Tikhonovsky MA, Pikalov AI, Sivtzov SV, Pirozhenko LA, et al. Influence of grain size on mechanical and corrosion properties of magnesium alloy for medical implants, Mater. Und Werkstofftechnik Entwicklung, Fert. Prüfung, Eig Und Anwendungen Tech Werkstoffe 2009;40:242–6.
[43] Ahmadkhaniha D, Fedel M, Sohi MH, Deflorian F. Corrosion behavior of severely plastic deformed magnesium based alloys: a review. Surf Eng Appl Electrochem 2017;53:439–48.
[44] McCafferty E. Introduction to corrosion science, Springer Science & Business Media. 2010.
[45] McCafferty E. Introduction to corrosion science. 2010. https://doi.org/10.1007/978-1-4419-0455-3.
[46] Ascencio M, Pekguleryuz M, Omanovic S. An investigation of the corrosion mechanisms of WE43 Mg alloy in a modified simulated body fluid solution: the influence of immersion time. Corrosion Sci 2014;87:489–503.
[47] Ascencio M, Pekguleryuz M, Omanovic S. An investigation of the corrosion mechanisms of WE43 Mg alloy in a modified simulated body fluid solution: the effect of electrolyte renewal. Corrosion Sci 2015;91:297–310.
[48] Mehdizade M, Soltanieh M, Eivani AR. Surface & Coatings Technology Investigation of anodizing time and pulse voltage modes on the corrosion behavior of nanostructured anodic layer in commercial pure aluminum. Surf Coating Technol 2019;358:741–52. https://doi.org/10.1016/j.surfcoat.2018.08.046.
[49] Mehdizade M, Eivani AR, Soltanieh M. Effects of reduced surface grain structure and improved particle distribution on pitting corrosion of AA6063 aluminum alloy. J Alloys Compd 2020;838:155464. https://doi.org/10.1016/j.jallcom.2020.155464.